IEEE Access
Multidisciplinary | Rapid Review | Open Access Journal

Received 27 October 2023, accepted 28 November 2023, date of publication 7 December 2023,
date of current version 18 December 2023.

Digital Object Identifier 10.1109/ACCESS.2023.3340433

RESEARCH ARTICLE

Control of Converter for a Solar PV-BESS Powered Telecom Load With Real, Reactive and Harmonic Power Exchange With Grid

V. SHEEJA[1], R. KALPANA[1], (Senior Member, IEEE), UMASHANKAR SUBRAMANIAM[2], (Senior Member, IEEE), AND DHAFER J. ALMAKHLES[2], (Senior Member, IEEE)

[1]National Institute of Technology, Karnataka, Surathkal, Mangaluru 575025, India
[2]Renewable Energy Laboratory, Communications and Networks Department, Prince Sultan University, Riyadh 11586, Saudi Arabia

Corresponding author: R. Kalpana (kalpana@nitk.edu.in)

The authors gratefully acknowledge the financial support provided by the DST-SERB, Govt. of India under the grant EEQ/2022/001003 and the funding provided by the National Institute of Technology Karnataka. The authors thank the Renewable Energy Lab, Prince Sultan University, Riyadh, for the technical support and guidance.

ABSTRACT Due to safety considerations and the challenges involved in tracking the maximum output of series-connected cells, solar photovoltaic (PV) arrays are generally operated at lower voltage levels. A multiport converter can be used to interface telecom DC loads, typically rated at 48 V and powered by PV arrays and battery energy storage system (BESS). The grid integration of the system improves reliability while lowering the BESS rating. This work proposes a sliding mode control-based power flow management controller that maintains the load voltage of a telecom DC load, allows maximum power extraction from the PV module, and facilitates power sharing with AC grid. A voltage source converter and a high-gain bidirectional converter exchange power with the AC grid. A second-order generalized integral algorithm-based voltage source converter control is provided to inject/absorb active power, reactive power, and eliminate the harmonics of the telecom AC load. Detailed simulation studies employing MATLAB software are performed to validate the functionality of the converter as well as the power flow management control. Moreover, the system's performance is evaluated using a laboratory-developed experimental prototype.

INDEX TERMS Telecom load, grid integration, sliding mode control, power flow management, solar PV system, multiport converter.

I. INTRODUCTION

Renewable energy-based technologies for powering telecommunication loads minimise the burden on the conventional grid while also helping to reduce environmental pollution. The grid and diesel generator based conventional telecom power stations are nowadays substituted with locally available renewable energy sources (RESs). It is possible to feed telecom power stations with multiple RESs, which are often rated at lower voltage levels, and integrate them into the grid using a suitable power electronic interface and a line frequency (LF) transformer [1]. The base transceiver station's (BTS) telecom DC load is typically rated for 48V. The telecom AC load consists of air-conditioning and other ancillary loads and are fed from the grid. To account for changes in PV power generation brought on by the environmental conditions, battery energy storage systems (BESS) are typically utilised to support solar PV systems [2], [3], [4].

The block diagram of a conventional telecom power supply that uses a BESS and a solar PV module is demonstrated in Fig. 1 (a). Grid integration of the PV-BESS system lowers the BESS rating and improves power supply dependability [5]. Fig. 1 (b) demonstrates a low voltage system with a multiport converter (MPC), that reduces power processing stages, thus increasing the system's overall efficiency [6]. MPCs

The associate editor coordinating the review of this manuscript and approving it for publication was Ali Raza.

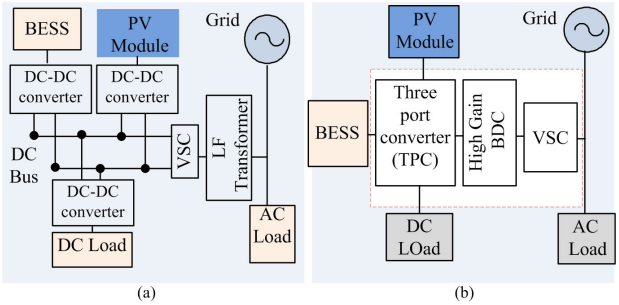

FIGURE 1. Block diagram of RESs based telecom power station (a) Conventional (b) Low volage DC bus system.

with high frequency (HF) transformer/coupled inductors for isolation and voltage boosting increase the circuit losses thereby reducing the efficiency compared to non-isolated converters. During switching transitions, the HF transformer's leakage inductance creates voltage spikes on semiconductor devices [7].

A closed loop system with a power flow management (PFM) is necessary to guarantee the MPC's functioning under dynamically varying solar irradiations. In order to address the mode switching problem associated with charging/discharging of energy storage system, a seamless control method using a proportional integral (PI) compensator has been discussed [8]. Anand et al. [9], proposed a PFM control for an MPC interfacing solar PV array, BESS, and a DC load demonstrating smooth power exchange from one mode to another. The power flow modes are determined by the solar PV system's maximum power point (MPP) and DC load voltage regulation using a PI controller.

In order to integrate the RES-based DC microgrid with the AC grid, the control algorithm needs to be equipped for synchronization with the AC voltage [10], [11]. Compared to multilevel inverters [12], the control complexity is reduced in voltage source converters [13]. A DC microgrid with a DC load, BESS, wind generator and a wave generator are integrated into the AC grid in [14] and a grid integrated solar PV based electric vehicle charging system in [15]. The PFM involves a PI compensator with a feedback system to maintain the DC load voltage. However, [16] discussed the synchronisation of voltage source converter (VSC) under grid disturbances including DC offsets, frequency fluctuations, voltage sag, swell, and harmonics using a generalised integral controller. The multifunctional operation for power quality improvement such as reactive power and harmonic compensation along with PV power injection to AC grid is also made possible. A microgrid system with a PV-BESS-diesel generator having a new adaptive filter control algorithm for frequency regulation and power quality improvement at the generator terminals is discussed [17]. The control is demonstrated for isolated power system. The control of a unified power quality conditioner in [18] facilitates real power injection from PV array to the grid along with power quality improvement. But, the system is not supporting low voltage DC grid. The grid integration of a solar PV system employing a cascaded H-bridge multilevel inverter using a damped second order generalised integral (SOGI) is demonstrated to be superior [19]. A fixed frequency SOGI control [20] phase locked loop is demonstrated. The system frequency may deviate during disturbances and hence a frequency adaptive SOGI gives better performance. The SOGI controllers discussed has utilised PI compensators for estimating control signals. Implementation of a sliding mode controller (SMC) was reported to be more accurate and stable during dynamic conditions of a standalone power generation system using hydro, wind and solar PV array [21]. SMC controller demonstrated in [22] is found to be better for estimating control signals for a solar PV array integrated multifunctional EV charger.

The energy management control of a four port converter having one input port, two bipolar outputs, and a battery port for a PV-BESS fed DC load system is demonstrated in [23]. The converter is suitable for a bipolar DC microgrid and is incapable of grid integration. Time multiplexed converter and control of a switched boost MPC having PV, BESS, and household DC loads are discussed [24]. Here also, a high voltage (HV) port is lacking for grid integration. Managing the power-sharing among the two input sources in a four-port converter has been demonstrated in [25] and grid integration is not possible with this configuration. A four port converter with unidirectional power flow to the HV port is discussed in [26]. It is not suitable for bidirectional power flow with HV port and has two coupled inductors for voltage boosting. A closed loop power flow management system is discussed in [27] for isolated load applications fed by a PV and BESS. The MPC has only unidirectional HV load port and has a coupled inductor for voltage boosting. A non-isolated multiport converter for grid integrated PV system demonstrates higher efficiency [28] but is having more inductors in the converter. A non-isolated bidirectional HV port for AC grid integration is presented in [29] with an MPC and is demonstrating power flow management control to extract MPP of PV array and to regulate DC load voltage under dynamic variations in PV power.

In this paper, a power flow management control is proposed for a PV-BESS- based low voltage power supply system for telecom load along with AC grid integration facilitating the real, reactive and harmonic power exchange with the AC grid. The system has the following merits;

- A robust and stable SMC-based controller is demonstrated for regulating the telecom DC load voltage with enhanced accuracy and improved dynamic performance.
- A single inductor-based multiport converter with reduced size and cost along with a non-isolated high gain bidirectional DC-DC converter (HGBC) developed and tested for the system.
- Control for the VSC is demonstrated with a frequency adaptive second-order generalized integral (SOGI) controller to compensate for the harmonic and reactive components of the AC supply current, ensuring improved power quality.

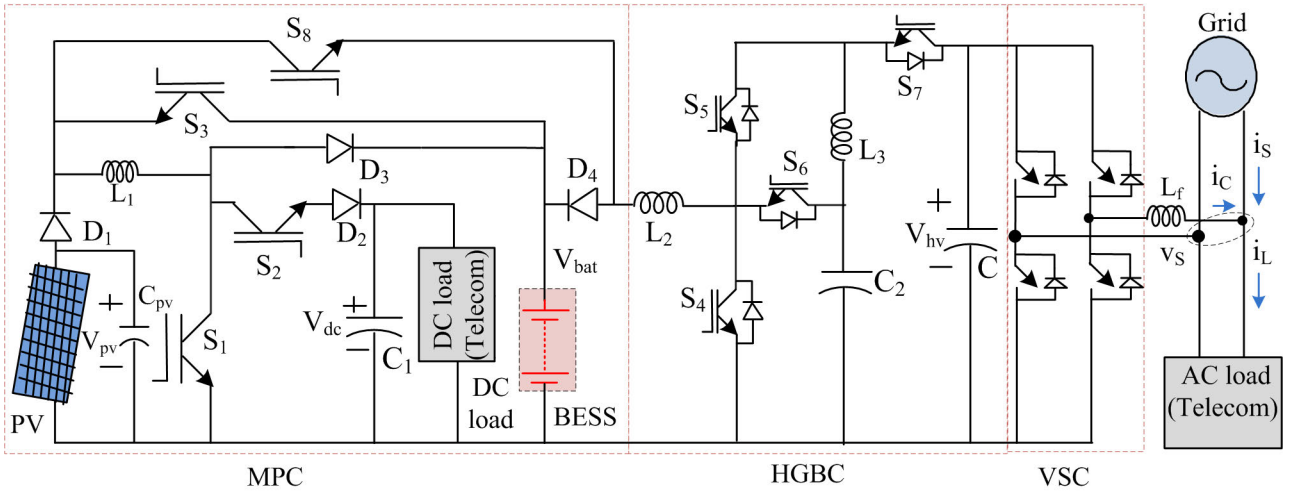

FIGURE 2. The converter configuration for a solar PV-BESS-based grid-integrated telecom power station.

- The DC load, BESS, and solar PV are operated at lower voltages, reducing the voltage stress on MPC switches and ensuring operational safety and effective power extraction from parallel connected PV modules.

The configuration of the system is discussed in Section II, and Section III provides a proposed control along with a power flow management algorithm. Section IV finally presents the results and related discussion.

II. CONFIGURATION OF THE SYSTEM

The converter configuration for a solar PV-BESS-based grid-integrated telecom power station is presented in Fig. 2. The PV, telecom DC load and BESS operate at lower voltages and are interfaced by an MPC to manage the power flow, while surplus PV power is given directly to the grid via the HGBC and VSC. The MPC is controlled by regulating switches S_1, S_2, and S_3 in time-shared mode and the HGBC is controlled by switches S_4 and S_5. If PV output is unavailable, the DC load and BESS are fed from the grid via the VSC and HGBC by controlling switches S_6 and S_7. The power sharing with the grid requires a high voltage (HV) at the DC link of VSC (V_{hv}) and is obtained by the HGBC. In order to avoid the operation of devices at extreme duty ratios, HGBC with a quadratic gain is used. By injecting a compensating current (i_c) with harmonics and reactive components of load current (i_L), the operation of VSC assures improved grid current (i_s) quality.

III. POWER FLOW MANAGEMENT AND CONTROL

The irradiance variation affects the PV power output and hence the power flow to/from BESS need to be controlled, as the DC load power is constant and is typically rated for 48V. When the solar irradiance is high, after feeding the telecom DC load, the additional power is fed to BESS and/or AC grid. When there is no or little solar irradiation, the BESS and/or grid provide the DC load requirement.

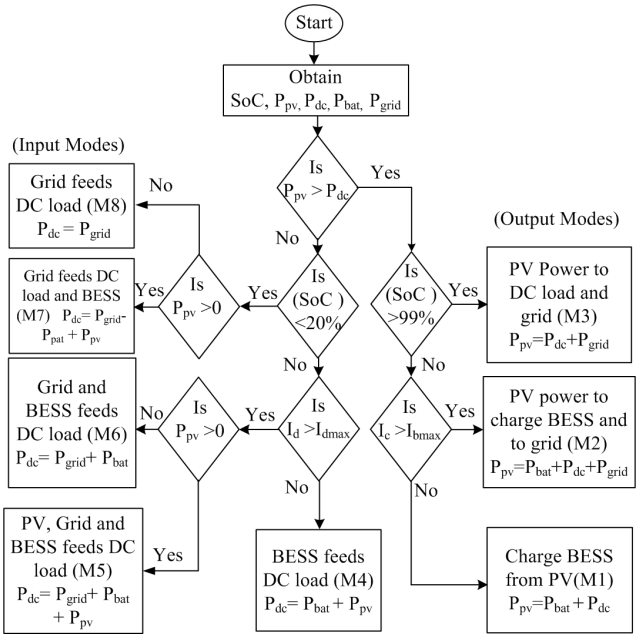

FIGURE 3. Power flow management (PFM) algorithm for the control of the system.

A. POWER FLOW MANAGEMENT ALGORITHM AND MODES OF OPERATION

A flow chart for the power flow management (PFM) algorithm is presented in Fig. 3. The PV power, P_{pv}, BESS power, P_{bat}, grid power, P_{grid}, DC load power, P_{dc} and state of charge (SoC) of BESS are sensed. When the amount of PV power available exceeds the requirement for telecom DC load, the PV feeds multiple outputs and are referred to as output modes. If the PV output is inadequate to satisfy the necessary DC load requirement, the modes are referred to as input modes. When excess PV power is available, it is used for feeding the DC load and charging the BESS. This operation is denoted as mode 1 (M1). If the BESS current

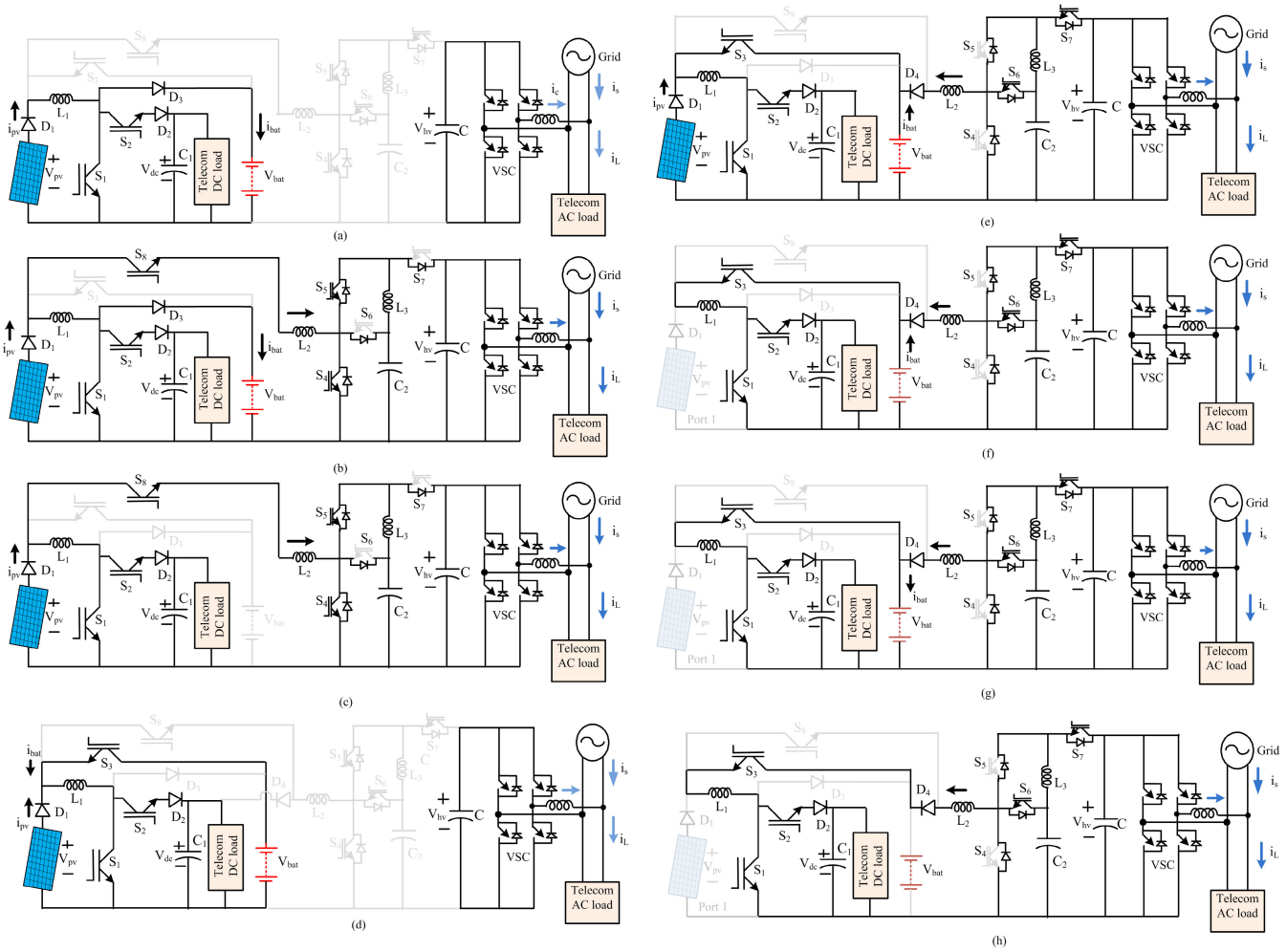

FIGURE 4. Modes of operation of the proposed configuration (a) M1 (b) M2 (c) M3 (d) M4 (e) M5 (f) M6 (g) M7 (h) M8.

exceeds the charging current limit, power is also transferred to the AC grid, denoting mode 2 (M2). The BESS stops charging when the SoC reaches its maximum capacity and supplies any excess power available to the AC grid in mode 3 (M3). When PV output is reduced, BESS discharges to satisfy the DC load requirement in mode 4 (M4). If the discharging current reaches its maximum limit, the AC grid supplies extra power to meet the DC load, denoting mode 5 (M5). If the BESS SoC falls below the minimum limit, the AC grid and PV will supply the DC load demand during mode 6 (M6). If the PV output is unavailable, grid and BESS support the DC load during mode 7 (M7), whereas the grid is the only source for the DC load during mode 8 (M8).

The topologies according to the various operating modes are illustrated in Fig. 4(a)-(h). Fig. 4(a)-(c) demonstrates operation during various output modes. During M1, switching devices S_1 and S_2 are modulated to manage the power flow to DC load and BESS, whereas the grid provides power to the telecom AC load as shown in Fig. 4(a). Here, VSC is used only for compensating the power quality issues. The inductor L_1 is charged and discharged in time shared mode to accomplish the power sharing between DC load and the BESS. The voltage across inductor L_1 is equated over a period and obtained the relation for DC load voltage (V_{dc}) as,

$$V_{dc} = [V_{pv} - V_{bat}(1 - d_1 - d_2)]/d_2 \quad (1)$$

The duty ratios of devices S_1 and S_2 are represented as d_1 and d_2, respectively. V_{pv} represents the solar PV voltage and V_{bat} is the BESS voltage. The period $(1-d_1-d_2)T$ represents the period at which the BESS is fed from the PV supply. Hence, $(d_1 + d_2) \leq 1$.

Fig. 4(b) illustrates the equivalent circuit for mode M2. Along with S_1 and S_2, S_4 and S_5 of HGBC is also operated inorder to obtain a sufficiently high voltage at the DC link of VSC, enabling power injection to the grid/AC load. Here, VSC is controlled for both real power injection and power quality compensation at the AC grid. Fig. 4(c) depicts the equivalent circuit during M3, where PV output is delivered to both DC load and AC grid when the BESS is completely charged. When the switches S_4 and S_5 of HGBC are pulse

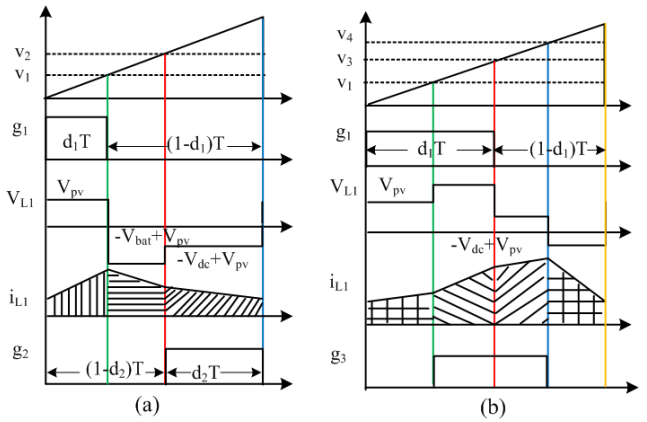

FIGURE 5. Key waveforms of the multiport converter (a) multiple output mode (b) multiple input mode.

width modulation (PWM) controlled with a duty ratio d_4, the equation for the voltage gain is,

$$\frac{V_{hv}}{V_{pv}} = \frac{1}{(1-d_4)^2} \tag{2}$$

Fig. 4(d)-(h) depicts various input modes of operation, if the PV output is less or absent. During M4, the inductor L_1 is charged and discharged in time-shared mode by the operation of S_1, S_2 and S_3 and is demonstrated in Fig. 4(d). The DC voltage (V_{dc}) during the input mode is obtained by equating voltage across inductor L_1 over a period as,

$$V_{dc} = [V_{pv}(1-d_3) + V_{bat}d_3]/(1-d_1) \tag{3}$$

where, d_3 represents the duty ratio of S_3. During M5, as shown in Fig. 4(e), the AC grid power is injected to the DC load through HGBC by operating devices S_6 and S_7 so that the DC link voltage (V_{hv}) is stepped down to the BESS voltage (V_{bat}). The equation for the voltage gain of HGBC for reverse operation is obtained as,

$$\frac{V_{bat}}{V_{hv}} = (d_6)^2 \tag{4}$$

where, d_6 represents the duty ratio of S_6 and S_7. The DC load requirement is met by the BESS and grid in M6, if PV output is unavailable, as demonstrated in Fig. 4(f). The grid charges the BESS in M7 (Fig. 4(g)) while supporting the DC load requirement, and the grid solely feeds the DC load in M8 (Fig. 4(h)). Fig. 5(a) and (b) represent the theoretical waveforms for the multiport converter during multiple output mode and multiple input mode.

The VSC is interfaced at the HV side of HGBC. The minimum DC link voltage of the VSC is selected as,

$$V_{hv} = 1.2\hat{V}_{ac}/m_a \tag{5}$$

where, $\hat{V}_{ac}$ denotes the AC voltage amplitude, and m_a is the modulation index. The factor 1.2 is used for compensating the voltage drop in switches and filters.

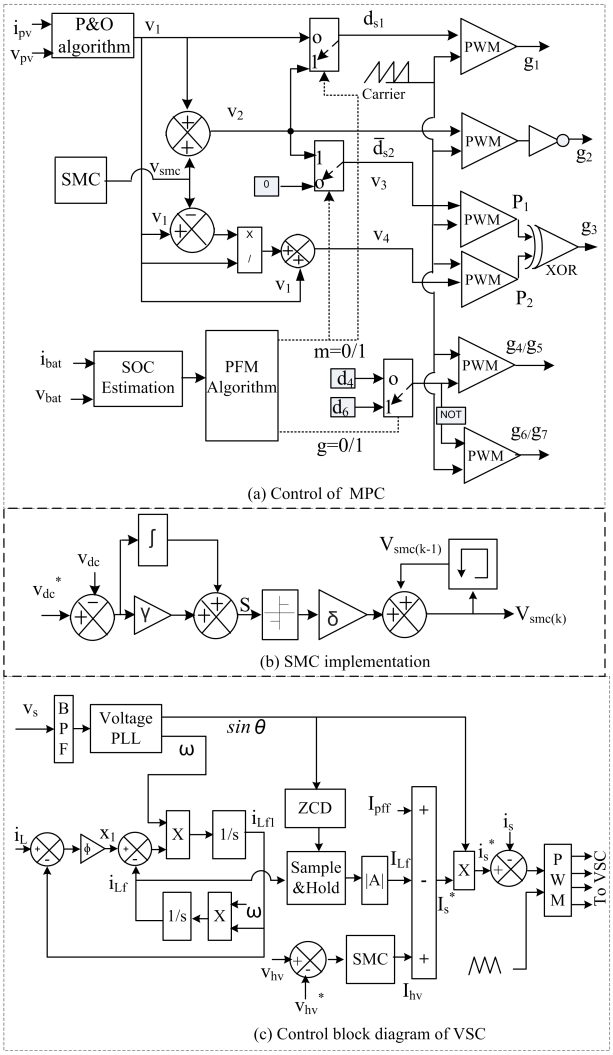

FIGURE 6. Proposed control block diagram for the control of MPC and VSC.

B. PROPOSED CONTROL ALGORITHM

The controller's objective is to ensure a reliable power supply to the telecom DC load despite the system's dynamic conditions. The performance in all operating modes is determined by how accurately the control algorithm regulates the DC load voltage. A sliding mode controller is designed to improve the accuracy during dynamic conditions so that the system performance is improved. As illustrated in Fig. 6(a), control of MPC involves MPP operation of the PV module using voltage (v_{pv}) and current (i_{pv}) signals. Here, MPP is estimated using a perturb and observe (P&O) approach, and the output is utilized as a signal (v_1) equivalent to the duty ratio of switch S_1 during the output mode. A sliding mode controller is implemented using the voltage error that is determined by the reference DC load voltage (v_{dc}*) and its actual value as in Fig. 6(b). A sliding surface S is defined with voltage error (v_e) as [22],

$$S = \gamma V_e + \int V_e dt \tag{6}$$

where, γ is a positive constant that governs the system's behaviour in both dynamic and steady-state situations. The voltage error v_e is given as,

$$V_e = (V_{dc}{}^* - V_{dc}) \tag{7}$$

The DC power may be expressed as,

$$P_{dc} = V_{dc}I_{dc} = V_{dc}C_1\frac{d}{dt}V_{dc} + \frac{1}{R_{dc}}V_{dc}{}^2 \tag{8}$$

$$\dot{V}_{dc} = \frac{I_{dc}}{C_1} - \frac{V_{dc}}{R_{dc}C_1} + \mu \tag{9}$$

where, μ is the disturbance in the system upper bounded by σ which is always less than 1. The DC load voltage controller is devised using the stability criteria $\lim_{s\to 0} S.\dot{S} < 0$.

$$\dot{S} = \gamma\dot{v_e} + v_e \tag{10}$$

$$S\dot{S} = S[\gamma(\dot{V_{dc}}{}^* - \dot{V_{dc}}) + (V_{dc}{}^* - V_{dc})] \tag{11}$$

$$S\dot{S} = S[-\gamma(\frac{I_{dc}}{C_1} - \frac{V_{dc}}{R_{dc}C_1} + \mu) + (V_{dc}{}^* - V_{dc})] \tag{12}$$

For $\dot{S}$ to be negative definite, it is sufficient that the following inequality holds,

$$\gamma[(\frac{I_{dc}}{C_1} - \frac{V_{dc}}{R_{dc}C_1} + \mu) + (V_{dc}{}^* - V_{dc})] > 0 \tag{13}$$

For $\dot{S}$ to be positive definite, it is sufficient that the following inequality holds,

$$\gamma[(\frac{I_{dc}}{C_1} - \frac{V_{dc}}{R_{dc}C_1} + \mu) + (V_{dc}{}^* - V_{dc})] < 0 \tag{14}$$

The inequalities in (13) and (14) defines the range of values and hence the values for sliding coefficients γ and μ are obtained. The values are given in Appendix.

The designed control law for v_{smc}, is shown in Fig. 6(b) and given as,

$$v_{smc(k)} = v_{smc(k-1)} + \delta sig(S) \tag{15}$$

where δ is a positive constant scalar factor. The signal $v_{smc(k-1)}$ is obtained from the previous sample and the signal $v_{smc(k)}$ is derived after obtaining signum The trajectory of the system states always points towards the sliding surface and the value of δ is selected to be less than the upper bound value. The value is given in Appendix. It accounts for the conduction time of diode D_3, which controls the BESS charging current. When switch S_1 is OFF, inductor L_1 discharges to the BESS and DC load in shared mode by conducting D_3 and S_2, respectively. Thus, the control signal v_2 is obtained as the sum of v_1 and v_{smc}. The control pulse g_2 for switch S_2 is the complement of the pulse produced using v_2.

The control pulses of switch S_3 is derived for BESS discharging, during the input mode. The proportion of time period which corresponds to BESS discharging is estimated as v_{smc}. Since the ON period of S_1 corresponds to charging of L_1 from PV and BESS, the control signal v_3 is considered as the sum of v_1 and v_{smc}. The pulse P_1 is produced using (v_3) that corresponds to the discharging current of the BESS. The signal v_4 is obtained as,

$$v_4 = v_1 + (v_1 - v_{smc})/v_1 \tag{16}$$

The signal v_4 is compared to a carrier signal to produce the second pulse, P_2. By the XOR operation of two pulses (P_1, P_2), the gating pulse for switch S_3 is generated. The power to AC load/grid is set by the algorithm, by selecting 0 or 1, as determined by the SoC of BESS. It is used to generate control pulse for S_4 (g_4) and S_5 (g_5) during output mode and control pulses (g_6, g_7 and g_8) for switches S_6, S_7 and S_8 while drawing power from the grid during input mode.

C. CONTROL ALGORITHM FOR THE VSC

The AC grid synchronisation algorithm presented in [20] is improved with a frequency adaptive second order generalised integral control instead of a fixed frequency one. The control algorithm used to operate the grid connected VSC is shown in Fig. 6(c). The objective is to exchange surplus or deficit real power with the grid after meeting the telecom AC load demand. Furthermore, the harmonics and reactive components of the AC load are compensated. It is required to sense the PCC voltage (v_S), DC link voltage (v_{hv}), grid current (i_S) and telecom AC load current (i_L). The fundamental component of sensed load current (i_{Lf}) is estimated using second order generalised integral control [19]. The equations for estimating fundamental component are,

$$i_{Lf1} = \int \omega(x_1 - i_{Lf})dt \tag{17}$$

$$x_1 = \phi(i_L - i_{Lf1}) \tag{18}$$

$$i_{Lf} = \int \omega i_{Lf1}dt \tag{19}$$

where ϕ is the gain factor which is always less than 2 and it is taken as 1.4 in this study. A phase-locked loop (PLL) is used to determine the frequency (ω) from the voltage signal. The amplitude of the fundamental component of load current (I_{Lf}) is obtained from a sample and hold unit in a zero-crossing detector (ZCD) using the template of voltage signal (u). The current to be injected/absorbed to the grid at the DC link of VSC, (I_{hv}), is estimated using a sliding mode controller. If the feed forward DC microgrid current is (I_{pff}), then the amplitude of reference grid current (I_s*) is obtained as,

$$I_s{}^* = I_{Lf} - I_{hv} + I_{pff} \tag{20}$$

Obtaining the reference grid current is as follows:

$$i_s{}^* = I_s{}^* sin\theta \tag{21}$$

The sensed grid current (i_s) is compared with reference grid current ($i_s{}^*$) and the error is processed in a PWM generator to generate constant frequency pulses for controlling the four switches of the VSC.

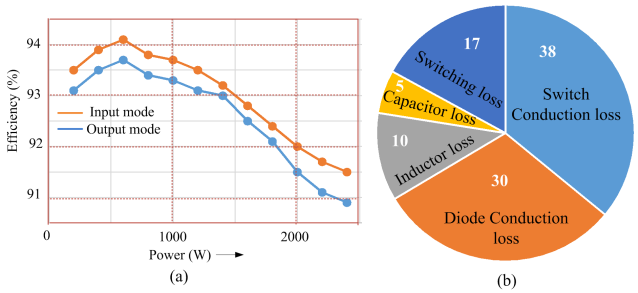

FIGURE 7. (a) Efficiency of MPC (b) Power loss components of MPC.

D. EFFICIENCY OF THE MPC

The converter efficiency during uotput and input operating modes are calculated as,

$$\eta(\%) = \frac{P_o}{P_o + P_L} * 100 \tag{22}$$

where P_o is output power and P_L is the power loss in MPC. Total power loss consists of conduction loss in the switches (P_{scond}), switching loss of the devices (P_{sw}), conduction loss in diodes(P_d), inductor loss(P_{ind}) and capacitor loss(P_{cap}).

$$P_L = P_{scond} + P_{sw} + P_d + P_{ind} + P_{cap} \tag{23}$$

The various loss are calculated as,

$$P_{scond} = \sum_{i=1}^{8} I_{Si}^2 r_{Si}; P_{sw} = \sum_{i=1}^{7} V_{si}^2 C_i f_{sw} \tag{24}$$

where $I_{Si}, r_{Si}, V_{si}, C_i, f_{sw}$ represents switch current, ON state resistance, stress, capacitance and switching frequency respectively.

$$P_{ind} = \sum_{i=1}^{3} I_{Li}^2 r_{Li}; P_d \quad = \sum_{i=1}^{5} I_{di}^2 R_i; P_{cap} = \sum_{i=1}^{3} I_{Ci}^2 r_{Ci} \tag{25}$$

where $I_{Li}, r_{Li}, I_{di}, R_i, I_{Ci}, r_{Ci}$ represents inductor current, inductor resistance, diode current, diode ON state resistance, capacitance current, capacitor resistance respectively. The Fig. 7 (a) shows the efficiency of the MPC during input mode and output mode and is comparatively high due to multiport operation. Morover, the components of power loss is depicted in Fig. 7 (b).

E. SMALL SIGNAL ANALYSIS

The stability of the system is analyzed by developing the state space averaged model of the MPC and by performing the small signal analysis. The state space averaged model for the MPC operating in the output mode is derived as,

$$\begin{bmatrix} di_{L1}/dt \\ dv_{pv}/dt \\ dv_{dc}/dt \end{bmatrix} = \begin{bmatrix} 0 & 1/L_1 & -dS_2/L_1 \\ 1/C_{pv} & 0 & 0 \\ dS_2/C_1 & 0 & -1/R_{dc}C_1 \end{bmatrix} \begin{bmatrix} i_{L1} \\ v_{pv} \\ v_{dc} \end{bmatrix} + \begin{bmatrix} dD_1/L_1 & 0 \\ 0 & 1/C_{pv} \\ 0 & 0 \end{bmatrix} \begin{bmatrix} v_{bat} \\ i_{pv} \end{bmatrix} \tag{26}$$

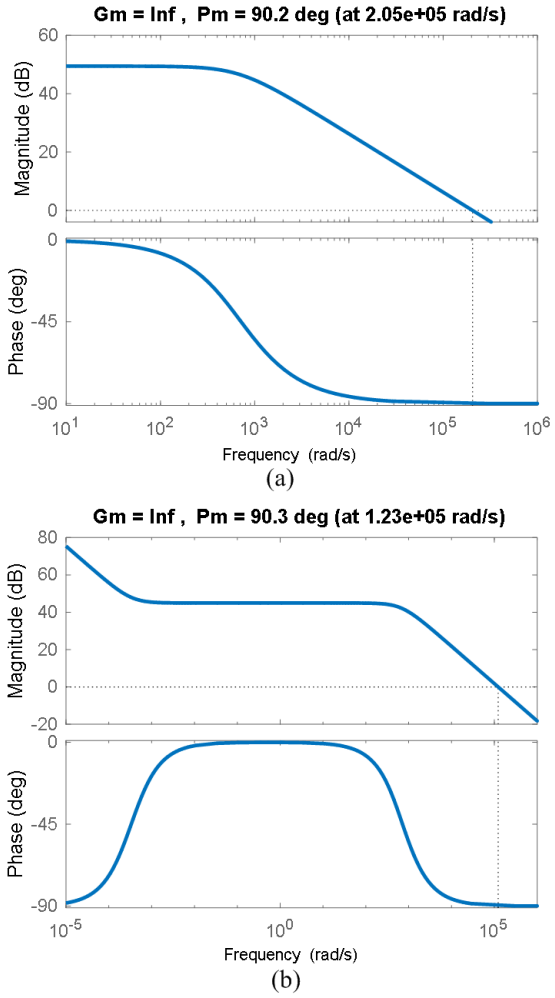

FIGURE 8. Bode plots of the system (a) without controller (b) with sliding mode controller.

where, R_{dc} is the DC load equivalent resistance. During any perturbation in the system, the system parameters are thought of as consisting of a steady state element and a small signal variable, as described in (27).

$$\begin{cases} i_{L1} = \bar{I}_{L1} + \hat{i}_{L1} \\ v_{pv} = \bar{V}_{pv} + \hat{v}_{pv} \\ v_{dc} = \bar{V}_{dc} + \hat{v}_{dc} \\ d_{S2} = \bar{d}_{S2} + \hat{d}_{S2} \end{cases} \tag{27}$$

Here, $\bar{I}_{L1}, \bar{V}_{dc}, \bar{V}_{pv}$, and $\bar{d}_{S2}$ represent respective steady state parts and $\hat{I}_{L1}, \hat{V}_{dc}, \hat{V}_{pv}$, and $\hat{d}_{S2}$ represent the small signal variables.

$$\begin{bmatrix} d\hat{i}_{L1}/dt \\ d\hat{v}_{pv}/dt \\ d\hat{v}_{dc}/dt \end{bmatrix} = \begin{bmatrix} 0 & 1/L & -d\bar{S}_2/L_1 \\ 1/C_{pv} & 0 & 0 \\ d\bar{S}_2/C_1 & 0 & -1/R_{dc}C_1 \end{bmatrix} \begin{bmatrix} \hat{i}_{L1} \\ \hat{v}_{pv} \\ \hat{v}_{dc} \end{bmatrix} + \begin{bmatrix} d\bar{D}_1/L_1 & 0 \\ 0 & 1/C_{pv} \\ 0 & 0 \end{bmatrix} \begin{bmatrix} \hat{v}_{bat} \\ \hat{i}_{pv} \end{bmatrix} + \begin{bmatrix} 0 & 0\,0 \\ 0 & 0\,0 \\ 1/C_1 & 0\,0 \end{bmatrix} \begin{bmatrix} \bar{I}_{L1} \\ \bar{v}_{pv} \\ \bar{v}_{dc} \end{bmatrix} [d\hat{S}_2] \tag{28}$$

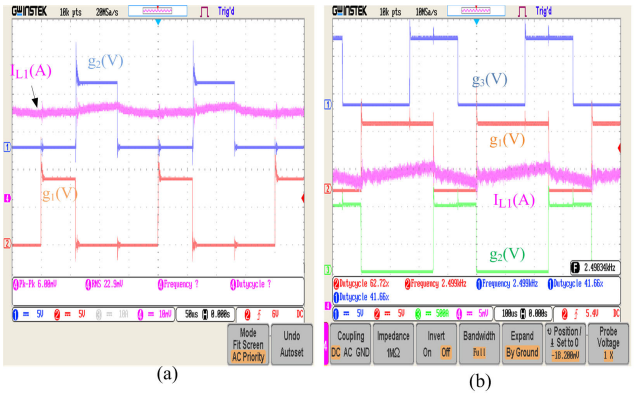

FIGURE 9. Experimental waveforms of the converter prototype: (a) Gate pulses g_1, g_2 and current through L_1 during multiple output mode (b) g_1, g_2, g_3 and current through L_1 during multiple input mode.

With the circuit values listed in the Appendix, the control transfer function for the converter is derived. The Bode diagram presented in Fig. 8(a) proves that the system is stable. The stability of the system with a sliding mode controller for regulating the DC voltage with a sliding surface $S > 0$ is also analysed. The Bode diagram for the system with the SMC is presented in Fig.8(b). According to the phase and gain margins determined from the Bode diagrams, closed-loop operations are found to be stable.

IV. RESULTS AND DISCUSSION

The system with a proposed power flow controller for a telecom load is modelled and simulated. Evaluations are made on the system's steady state and dynamic behaviour. Additionally, an experimental setup is developed and evaluated. The following sections contain an in-depth presentation of the findings. The Appendix includes a list of the proposed system's parameters.

A. STEADY STATE PERFORMANCE OF THE SYSTEM

The evaluation of the power flow controller is demonstrated during multiple output and input modes. The voltages and currents of inductors and switching pulses of the converter is shown in Fig. 9 (a)-(b). The switching pulses to S_1 (g_1), S_2 (g_2) and the inductor current (i_{L1}) during multiple output modes are shown in Fig. 9(a). Similarly, multiple input operation of the system is tested and gate pulses to $S_1(g_1)$, $S_2(g_2)$, $S_3(g_3)$ and the inductor current (i_{L1}) are depicted in Fig. 9(b). The PV voltage, V_{pv}, BESS voltage, V_{bat}, HV side voltage, V_{hv}, telecom DC load voltage, V_{dc} are depicted in Fig. 10(a). The inductor voltage, (v_{L1}) and current, (i_{L1}) during multiple output operation are depicted in Fig. 10(b). The single inductor based multiple output operation is verified by the multiple slopes during the discharging period.

B. DYNAMIC PERFORMANCE OF THE SYSTEM

The system's dynamic performance for input mode transitions is exhibited as shown in Fig. 11. The PV module and

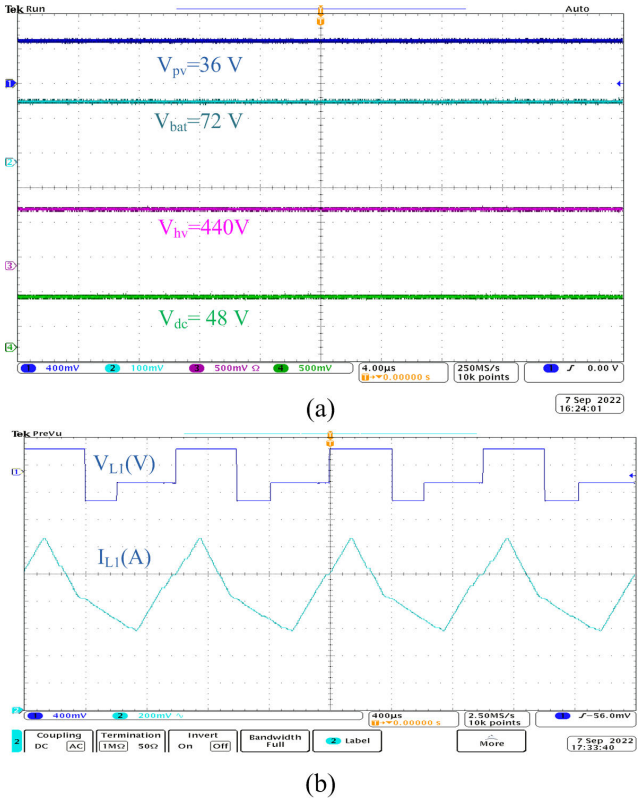

FIGURE 10. Experimental results during steady state operation (a) PV voltage, V_{pv}(50 V/div), BESS voltage, V_{bat}(50 V/div, HV side voltage, V_{hv} (300 V/div), telecom DC load voltage, V_{dc} (50 V/div) (b) Inductor voltage (v_{L1}) (50 V/div) and current (i_{L1}) (0.5A/div).

BESS are initially used to supply the DC load (M4). The DC load power is fulfilled by discharging the BESS as the PV power drops to 574.5 W at 0.5 seconds (618 W). It is shown that the grid, BESS, and PV are able to satisfy the DC load at 1.0 seconds (M5). After the BESS stops discharging at 1.26 seconds (due to the SoC hitting its lower limit), it continues to operate in M7, and after 2.0 seconds, the grid solely supplies the DC load (M8). The SMC controller, as depicted in fig.11 (b), regulates the voltage of the DC load to the reference value.

The system's performance is proven for output mode transitions, as illustrated in Fig. 12. Initially, the PV is powering both the BESS and the DC load (M1). The PV output increases at 0.8 seconds, and it can be observed that the extra power is fed to the BESS and grid (M2). The BESS stops charging at 1.3 seconds due to the SoC hitting its upper limit, and the power is transferred to grid (M3). The PV power increase at 2.0 seconds is supplied to the grid. The SMC controller, as depicted in Fig. 12 (b), regulates the voltage at the DC load to the required value. In order to compare, the proposed power flow management is implemented using a proportional integral (PI) controller. The PI controller parameters K_p and K_i are given in Appendix. Three transition uncertainties are applied at 0.8 s, 1.3 s and 2.0 s as shown in Fig. 12 (c). The uncertainties are depicted

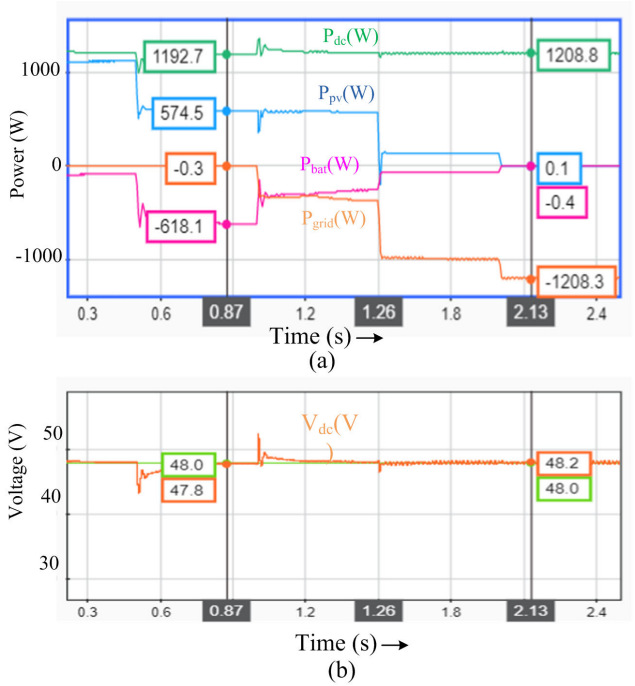

FIGURE 11. Simulation results during mode transitions in input modes (a) PV power, P_{pv}, BESS power, P_{bat}, grid power, P_{grid}, DC load power, P_{dc} (b) DC load voltage, V_{dc} and its reference value.

TABLE 1. Performance Comparison of SMC and PI Controllers.

	0.8 s		1.3 s		2.0 s	
	M_p(%)	t_s(s)	M_p(%)	t_s(s)	M_p(%)	t_s(s)
SMC	0.5	0.007	0.53	0.01	0.31	0.005
PI	1.04	0.2	3.96	0.3	0.83	0.03

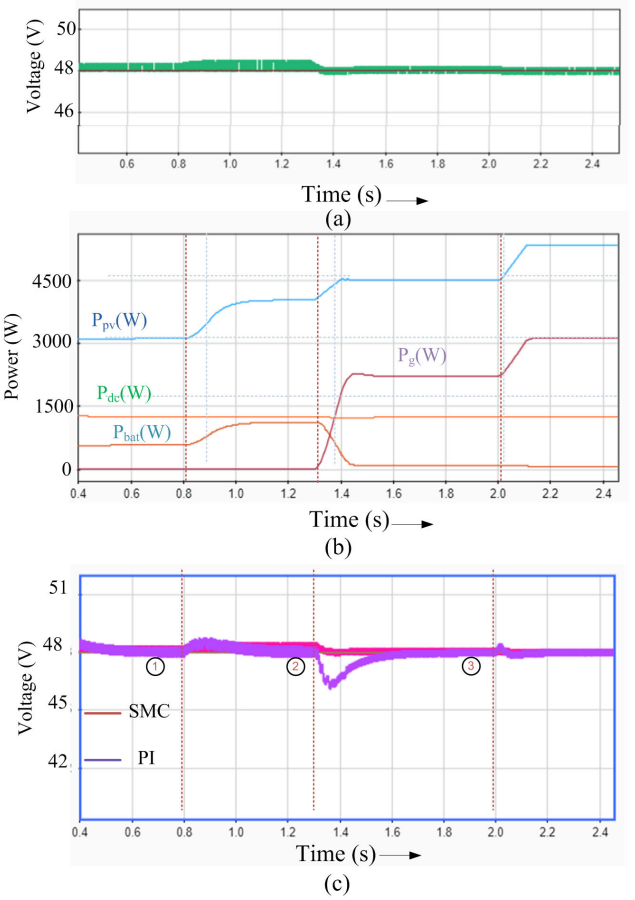

FIGURE 12. Simulation results during mode transitions in output modes (a) DC load voltage, V_{dc} (b) PV power, P_{pv}, BESS power, P_{bat}, grid power, P_{grid}, DC load power, P_{dc} (c) DC load voltage, V_{dc} using SMC and PI controllers.

in Fig. 12 (b). At 0.8 s, the solar PV power is increased and the SMC performance is superior in terms of maximum percentage deviation from the reference value (M_p) and the settling time (t_s). At instant 1.3 s, the system is subjected to two disturbances; the increase in PV power and reduction in BESS power. The SMC controller shows better performance as shown in Fig. 12 (b), where the PI controller response has a large deviation from the reference value and longer settling time. Similarly, at 2.0 s, the PV power is increased and the SMC is robust against all uncertainties. The performance during the uncertainties are tabulated in Table 1 and shows that the performance parameters are improved with sliding mode controller.

The experimental results of output mode operation are presented in Figs. 13 and 14. The PV current, I_{pv}, BESS current, I_{bat}, HV side current, I_{hv}, telecom DC load voltage, V_{dc} are shown in Fig. 13(a). The PV power, P_{pv}, BESS power, P_{bat}, grid power, P_{grid}, DC load power, P_{dc} are shown in Fig. 13(b). It is observed that the PV power generated is fed to the telecom DC load, BESS and telecom AC load. When the PV power is increased at a time instant, the excess power is absorbed by the BESS. The sliding mode controller controls the telecom DC load voltage to the reference value. The experimental results of input operation mode are presented in Fig. 14. For demonstrating the performance during input modes, solar PV power output is decreased and the corresponding variations in BESS power are observed. The PV current, I_{pv}, BESS current, I_{bat}, HV side current, I_{hv}, telecom DC load voltage, V_{dc} are shown in Fig. 14(a). The PV power, P_{pv}, BESS power, P_{bat}, grid power, P_{grid}, DC load power, P_{dc} are depicted in Fig. 14(b). Initially, telecom DC load requirement is met by PV, grid and BESS power. When the solar PV output is reduced, the BESS provides additional power to supply the DC load requirement. It is seen that the sliding mode controller regulates the DC load voltage to the reference value during disturbances in the system. The performance of the system during grid interaction for harmonic compensation, power absorption from the grid, and power injection to the grid are shown in Figs. 15-17. The real power absorption along with harmonic compensation is demonstrated in Fig. 15 (a), using PCC voltage (v_S), AC load current (i_L), grid current (i_S), VSC current (i_C). The real power injection along with harmonic compensation is presented in Fig. 15 (b), demonstrating the active power injection to the grid along with harmonic compensation

TABLE 2. Comparison of RES based power supply system.

Reported Systems	RESs	Features of MPC	RES Voltage	HV DC link Voltage	Type of HGBC	Features of Grid Integration	Features of PFM control
Tian et.al [23]	PV	3 unidirctional port, 1 bidirectional port	10-35 V	24 V	No	Not connected	Voltage regulation MPPT
Mishra et.al [24]	PV	2 unidirctional port, 1 bidirectional port	24 V	48 V	No	Not connected	Time multiplexed MPPT
Suresh et.al [25]	PV	1 input port, 1 bidirectional port	20 V	69 V	No	Not connected	PI controller MPPT
Zeng et.al [26]	PV, Wind	2 input ports, 1 bidirectional port	60 V	180 V	HF transformer Unidirectional	Not connected	Voltage regulation MPPT
Mansor et.al [18]	PV	1 input port 1 bidirectional port	39.8 V	700 V	Not applicable	Grid connected as UPQC	MPPT
Dipankar et.al [27]	PV	1 input port, 1 bidirectional port	35 V	350-460 V	HF transformer,	Active power	MPPT
Vivek et.al [17]	PV	1 input port, 1 bidirectional port	380 V	380 V	Not applicable	Active power, PQ enhancement	MPPT
Proposed System	PV	1 input port, 1 bidirectional port	35 V	440 V	Non-isolated HG Bidirectional	Active power, PQ enhancement	sliding mode control SOGI based extraction

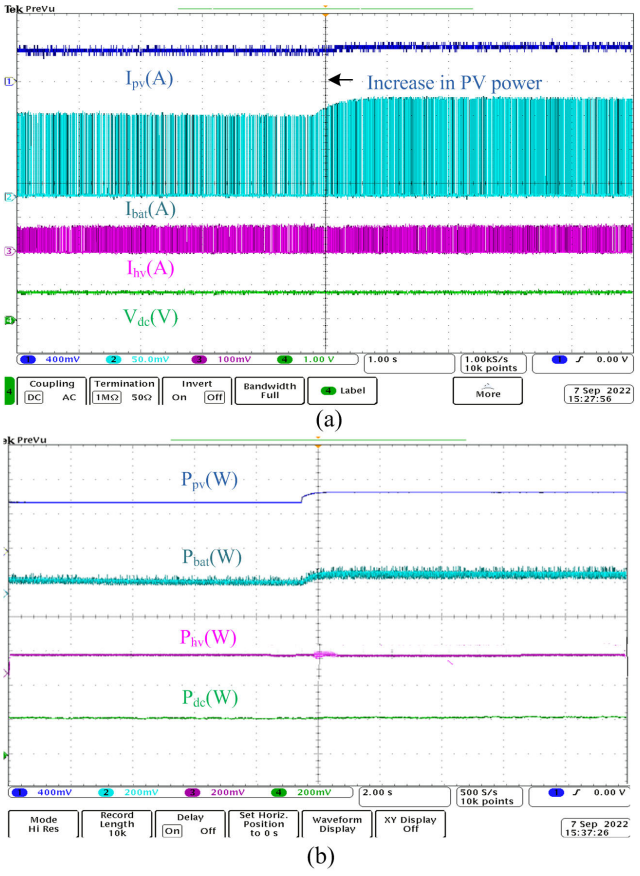

FIGURE 13. Experimental results for multiple output modes (a) The PV current, I_{pv}(50 A/div), BESS current, I_{bat} (5 A/div), HV side current, I_{hv} (5 A/div), telecom DC load voltage, V_{dc}(50 V/div) (b) PV power, P_{pv}(1kW/div), BESS power, P_{bat}(1kW/div), grid power, P_{grid}(1kW/div), DC load power, P_{dc} (1kW/div).

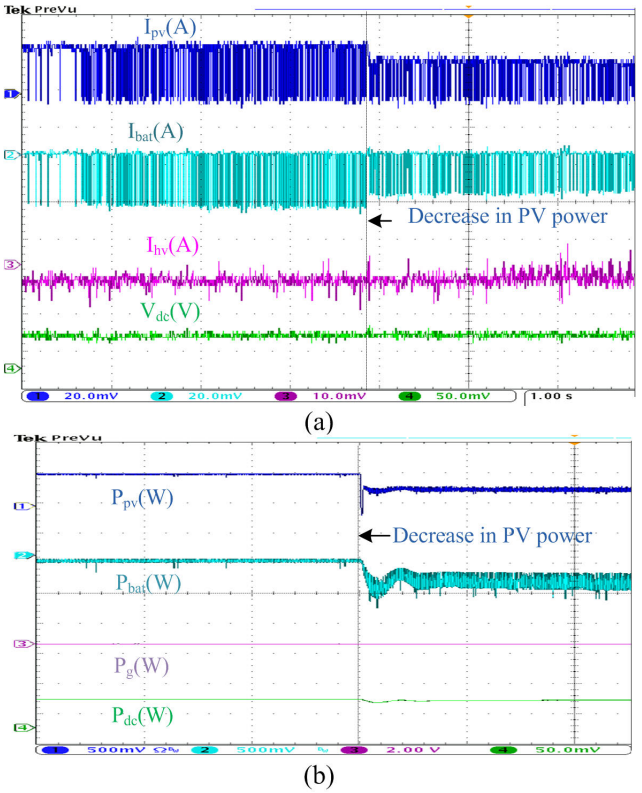

FIGURE 14. Experimental results for multiple input modes (a) The PV current, I_{pv} (10A/div), BESS current, I_{bat} (10A/div), HV side current, I_{hv} (10A/div), telecom DC load voltage, V_{dc} (50V /div) (b) PV power, P_{pv}(1kW/div), BESS power, P_{bat}(1kW/div), grid power, P_{grid} (1kW/div), DC load power, P_{dc}(1kW/div).

by the VSC. The AC grid current magnitude is in phase opposition to grid voltage, which shows the excess power injection to the grid. Moreover, harmonic compensation is demonstrated in Fig. 16 showing PCC voltage (v_S), VSC current (i_C), grid current (i_S) and AC load current (i_L), harmonic spectrum of grid current and harmonic spectrum of load current. While the load current is almost a square wave current, the grid current is found to be nearly sinusoidal. The load current THD is 40.62% whereas the grid current THD is reduced to 3.44%, within the limit specified by IEEE 519 [30]. The SOGI based VSC controller estimated the fundamental component of the load current precisely and only this fundamental is drawn from the grid. The harmonic

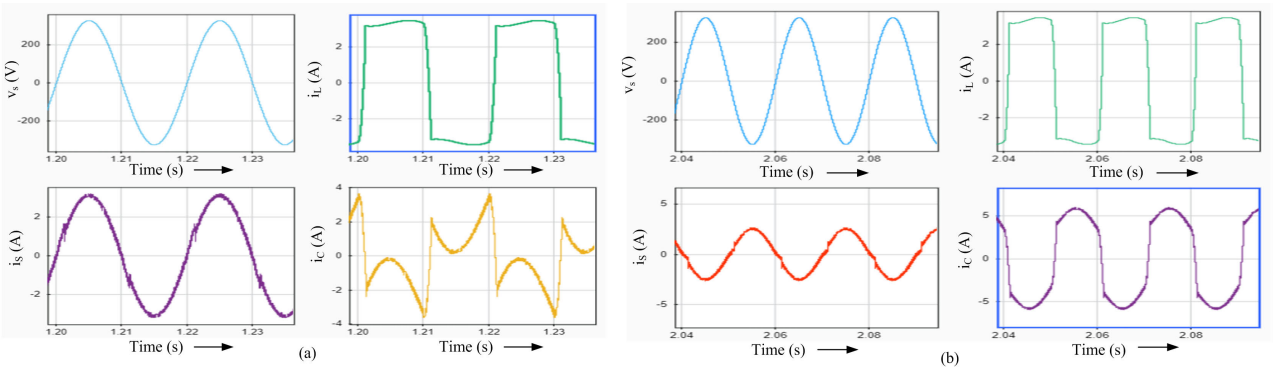

FIGURE 15. Steady state performance of the VSC (a) Real power absorption along with reactive and harmonic compensation showing PCC voltage (v_S), AC load current (i_L), grid current (i_S) and VSC current (i_C) (b)Real power injection along with reactive and harmonic compensation showing PCC voltage (v_S), AC load current (i_L), grid current (i_S) and VSC current (i_C).

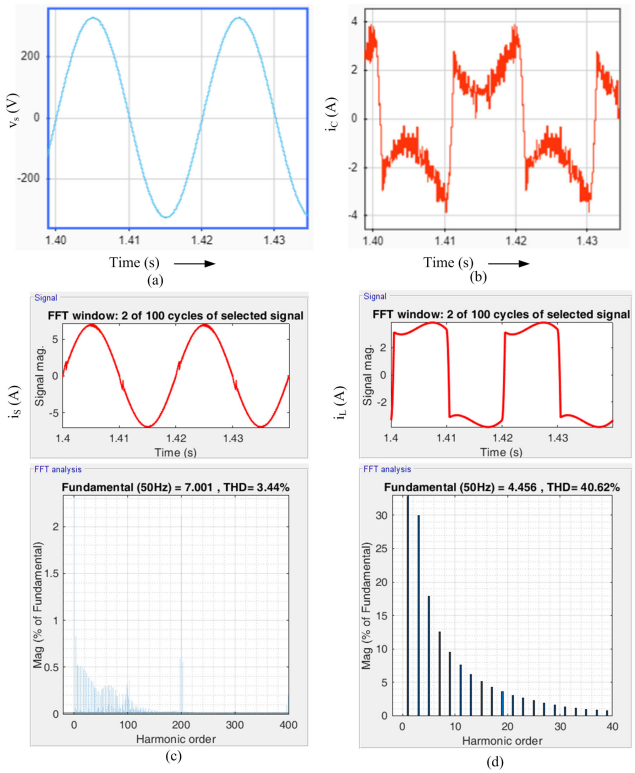

FIGURE 16. Harmonic compensation of VSC (a) PCC voltage (v_S), (b) VSC current (i_C), (c) grid current (i_S) along with harmonic spectrum and (d) AC load current (i_L) along with harmonic spectrum.

components and reactive component are supplied by the high frequency PWM controlled VSC, thus effectively mitigating power quality issues at the PCC.

The performance of VSC for reactive power and harmonic elimination along with active power injection is demonstrated in Fig. 17 (a) and (b). The AC grid voltage, telecom AC load current, the current drawn from the grid and the VSC current are demonstrated in Fig. 17 (a). The enlarged waveforms are shown in Fig. 17 (b). The grid current is observed to be sinusoidal whereas the load current is nearly a square wave current, demonstrating the harmonic compensation by the VSC. A photo of the experimental setup with MPC elements,

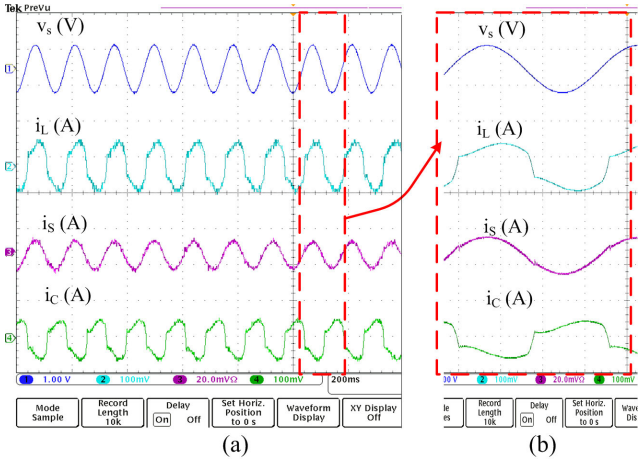

FIGURE 17. (a) Experimental performance of harmonic compensation using VSC: Grid voltage (300V/div), Grid current (5A/div), Load current(5A/div) and VSC current (5A/div) (b) Enlarged waveforms.

PV emulator, DC load, BESS and dSPACE control system is given in Fig. 19.

C. VERIFICATION OF MPP OPERATION

The MPP operation of the PV array is verified from the operating points and are given in Fig. 18. It is observed that the PV array is operated at different irradiation levels of 0.5 kW/m^2, 0.75 kW/m^2, and 0.9 kW/m^2 and the corresponding powers of PV array are 2200 W, 4000 W and 5300 W respectively as shown in Fig. 18(a). It is clear from Fig. 18(b) that the irradiance level is changed at time instants of 0.8s and 1.3s. The DC bus voltage is regulated by the system and the power produced by PV array is controlled very close to maximum power points of 2200 W, 4000 W and 5300 W at insolation levels of 0.5 kW/m^2, 0.75 kW/m^2, and 0.9 kW/m^2 respectively, verifying the MPP operation of the PV array.

D. COMPARISON OF THE PROPOSED SYSTEM

The proposed system is compared with some recent literatures on RES based power supply systems, as shown in

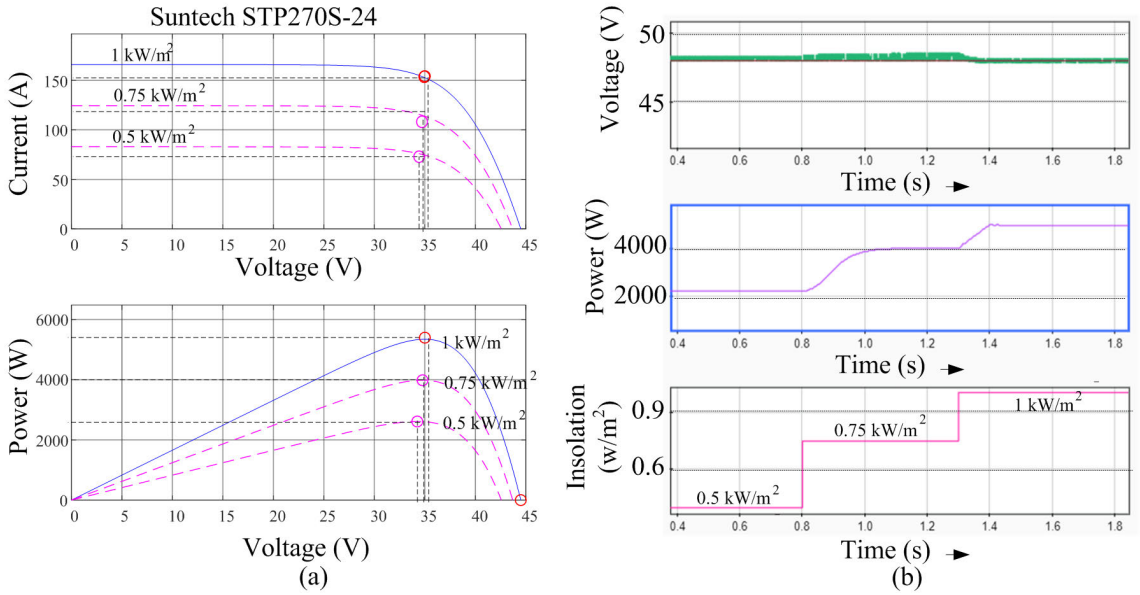

FIGURE 18. Performance of the MPP operation: (a) I-V curve and P-V curve of the PV array with operating points (b) DC bus voltage, PV power output and Solar insolation.

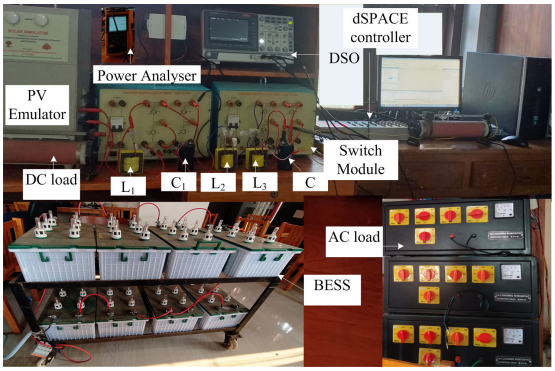

FIGURE 19. Experimental setup.

Table 2. Most of the systems are PV based with a BESS and feeding a DC load [23], [24], [25], where the PV is operating at a low voltage to enhance the safety and to avoid issues related to series connected PV arrays. Zeng et al. [26] used an HF transformer for interfacing with an HV DC load, whereas a UPQC is used in [18] to enhance the power quality at the PCC along with real power injection to the grid. Dipankar et. al [27] is demonstrating a PV-BESS integration system that has only unidirectional power flow with the grid. Vivek et al. [17] suggest a control algorithm for active power absorption from DG system along with power quality enhancement, in which PV is rated at a higher voltage. In the proposed system, the PV array is operating at a lower voltage and an efficient non-isolated HGBC is used for interfacing with the grid for real, reactive and harmonic compensation. SMC-based control for the voltage regulation of telecom DC load and a SOGI algorithm for power quality enhancement at the grid side are the additional benefits of the proposed system.

V. CONCLUSION

An SMC-based power flow controller is demonstrated for a grid-PV-BESS interfaced converter system feeding a telecom load. The performance of the system was satisfactory as evidenced by the regulation of the telecom DC load voltage with reduced overshoot and settling time under dynamic variations in solar PV power. A non-isolated HGBC and a single inductor-based multiport converter are developed and tested for the system. A frequency adaptive SOGI controller is demonstrated for the control of VSC, compensating reactive power and harmonics of the telecom AC load along with real power exchange with grid/AC load. It is observed that the total harmonic distortion of the grid current is maintained within the standards prescribed by IEEE 519.

As the multiport converter interfaced with PV-BESS-telecom DC load is operated at low voltage, the voltage stress on switches is reduced, ensuring safety in operation and effective power extraction from parallel connected PV arrays. As the power flow with the grid is bidirectional, the capacity of the BESS required is less, thus reducing the overall cost of the system. Using MATLAB software, thorough simulation studies are carried out to analyse and verify the system's various operational modes. The system's hardware prototype also is developed and verified in the laboratory. The system's performance is evaluated and found to be agreeing with simulation and theoretical studies.

APPENDIX A
SYSTEM PARAMETERS

PV Module with V_{pv}: 35V, I_{pv}: 154 A, P_{pv}: 5390 W;
Telecom DC load: 48 V, 1200 W; BESS: 72 V, 100 Ah;
Telecom AC load: 230V, 1500W, Single phase uncontrolled rectifier.

Inductors: L_1: 5.1 mH, L_2:1.60 mH, L_3:1.6 mH,
Capacitors: C_1: 0.75 mF; C_2:0.77 mF; C : 600 μF; C_{pv} : 900 μF.

APPENDIX B
CONTROL SYSTEM PARAMETERS

Sliding Mode Control Parameters: $\gamma = 0.1$, $\mu = 0.01$, $\delta = 0.0001$
Proportional-Integral control parameters: $K_p = 0.1, K_i = 0.01$
SOGI parameters: $\phi = 1.4$

REFERENCES

[1] O. C. Onar, O. H. A. Shirazi, and A. Khaligh, "Grid interaction operation of a telecommunications power system with a novel topology for multiple-input buck-boost converter," *IEEE Trans. Power Del.*, vol. 25, no. 4, pp. 2633–2645, Oct. 2010.
[2] J. S. Goud and R. Kalpana, "Optimal sizing of hybrid power supply system for telecommunication BTS load to ensure reliable power at lower cost," in *Proc. IEEE Int. Conf. Technol. Advancements Power Energy*, Dec. 2017, pp. 1–6.
[3] B. Mangu and B. G. Fernandes, "Efficiency improvement of solar-wind based dual-input Cuk-SEPIC converter for telecom power supply," in *Proc. 38th Annu. Conf. IEEE Ind. Electron. Soc.*, Oct. 2012, pp. 978–983.
[4] M. I. Hlal, V. K. Ramachandaramurthy, A. Sarhan, A. Pouryekta, and U. Subramaniam, "Optimum battery depth of discharge for off-grid solar PV/battery system," *J. Energy Storage*, vol. 26, Dec. 2019, Art. no. 100999, doi: 10.1016/j.est.2019.100999.
[5] N. R. Deevela, B. Singh, and T. C. Kandpal, "Load profile of telecom towers and potential renewable energy power supply configurations," in *Proc. IEEE Int. Conf. Power Electron., Drives Energy Syst. (PEDES)*, Dec. 2018, pp. 1–6.
[6] H. Moradisizkoohi, N. Elsayad, and O. A. Mohammed, "A family of three-port three-level converter based on asymmetrical bidirectional half-bridge topology for fuel cell electric vehicle applications," *IEEE Trans. Power Electron.*, vol. 34, no. 12, pp. 11706–11724, Dec. 2019.
[7] Z. Wang, Q. Luo, Y. Wei, D. Mou, X. Lu, and P. Sun, "Topology analysis and review of three-port DC–DC converters," *IEEE Trans. Power Electron.*, vol. 35, no. 11, pp. 11783–11800, Nov. 2020.
[8] M. Kwon and S. Choi, "Control scheme for autonomous and smooth mode switching of bidirectional DC–DC converters in a DC micro-grid," *IEEE Trans. Power Electron.*, vol. 33, no. 8, pp. 7094–7104, Aug. 2018.
[9] I. Anand, S. Senthilkumar, D. Biswas, and M. Kaliamoorthy, "Dynamic power management system employing a single-stage power converter for standalone solar PV applications," *IEEE Trans. Power Electron.*, vol. 33, no. 12, pp. 10352–10362, Dec. 2018.
[10] M. F. Elmorshedy, H. U. R. Habib, M. M. Ali, M. J. Sathik, and D. J. Almakhles, "Improved performance of hybrid PV and wind generating system connected to the grid using finite-set model predictive control," *IEEE Access*, vol. 10, pp. 110344–110361, 2022, doi: 10.1109/ACCESS.2022.3214996.
[11] K. Dhibi, M. Mansouri, K. Abodayeh, K. Bouzrara, H. Nounou, and M. Nounou, "Interval-valued reduced ensemble learning based fault detection and diagnosis techniques for uncertain grid-connected PV systems," *IEEE Access*, vol. 10, pp. 47673–47686, 2022, doi: 10.1109/ACCESS.2022.3167147.
[12] S. Ghoudelbourk, A. T. Azar, D. Dib, and A. Omeiri, "Selective harmonic elimination strategy in the multilevel inverters for grid connected photovoltaic system," *Int. J. Adv. Intell. Paradigms*, vol. 15, no. 3, p. 317, 2020, doi: 10.1504/ijaip.2020.105826.
[13] B. Singh, A. Chandra, and K. Al-Haddad, *Power Quality: Problems and Mitigation Techniques*. London, U.K.: Wiley, 2015.
[14] S.-Y. Lu, L. Wang, T.-M. Lo, and A. V. Prokhorov, "Integration of wind power and wave power generation systems using a DC microgrid," *IEEE Trans. Ind. Appl.*, vol. 51, no. 4, pp. 2753–2761, Jul. 2015.
[15] P. Prem, P. Sivaraman, J. S. S. Raj, M. J. Sathik, and D. Almakhles, "Fast charging converter and control algorithm for solar PV battery and electrical grid integrated electric vehicle charging station," *Automatika*, vol. 61, no. 4, pp. 614–625, Oct. 2020, doi: 10.1080/00051144.2020.1810506.
[16] R. Panigrahi, S. K. Mishra, S. C. Srivastava, A. K. Srivastava, and N. N. Schulz, "Grid integration of small-scale photovoltaic systems in secondary distribution network—A review," *IEEE Trans. Ind. Appl.*, vol. 56, no. 3, pp. 3178–3195, May 2020.
[17] V. Narayanan, S. Kewat, and B. Singh, "Control and implementation of a multifunctional solar PV-BES-DEGS based microgrid," *IEEE Trans. Ind. Electron.*, vol. 68, no. 9, pp. 8241–8252, Sep. 2021.
[18] M. A. Mansor, K. Hasan, M. M. Othman, S. Z. B. M. Noor, and I. Musirin, "Construction and performance investigation of three-phase solar PV and battery energy storage system integrated UPQC," *IEEE Access*, vol. 8, pp. 103511–103538, 2020.
[19] C. M. N. Mukundan, P. Jayaprakash, U. Subramaniam, and D. J. Almakhles, "Binary hybrid multilevel inverter-based grid integrated solar energy conversion system with damped SOGI control," *IEEE Access*, vol. 8, pp. 37214–37228, 2020.
[20] F. Xiao, L. Dong, L. Li, and X. Liao, "A frequency-fixed SOGI-based PLL for single-phase grid-connected converters," *IEEE Trans. Power Electron.*, vol. 32, no. 3, pp. 1713–1719, Mar. 2017.
[21] U. K. Kalla, B. Singh, S. S. Murthy, C. Jain, and K. Kant, "Adaptive sliding mode control of standalone single-phase microgrid using hydro, wind, and solar PV array-based generation," *IEEE Trans. Smart Grid*, vol. 9, no. 6, pp. 6806–6814, Nov. 2018.
[22] A. Verma, B. Singh, A. Chandra, and K. Al-Haddad, "An implementation of solar PV array based multifunctional EV charger," *IEEE Trans. Ind. Appl.*, vol. 56, no. 4, pp. 4166–4178, Jul. 2020.
[23] Q. Tian, G. Zhou, M. Leng, G. Xu, and X. Fan, "A nonisolated symmetric bipolar output four-port converter interfacing PV-battery system," *IEEE Trans. Power Electron.*, vol. 35, no. 11, pp. 11731–11744, Nov. 2020.
[24] S. K. Mishra, K. K. Nayak, M. S. Rana, and V. Dharmarajan, "Switched-boost action based multiport converter," *IEEE Trans. Ind. Appl.*, vol. 55, no. 1, pp. 964–975, Jan. 2019.
[25] K. Suresh, C. Bharatiraja, N. Chellammal, M. Tariq, R. K. Chakrabortty, M. J. Ryan, and B. Alamri, "A multifunctional non-isolated dual input-dual output converter for electric vehicle applications," *IEEE Access*, vol. 9, pp. 64445–64460, 2021.
[26] J. Zeng, J. Ning, X. Du, T. Kim, Z. Yang, and V. Winstead, "A four-port DC–DC converter for a standalone wind and solar energy system," *IEEE Trans. Ind. Appl.*, vol. 56, no. 1, pp. 446–454, Jan. 2020.
[27] D. Debnath and K. Chatterjee, "Two-stage solar photovoltaic-based stand-alone scheme having battery as energy storage element for rural deployment," *IEEE Trans. Ind. Electron.*, vol. 62, no. 7, pp. 4148–4157, Jul. 2015.
[28] V. Sheeja, R. Kalpana, B. Singh, U. Subramaniam, and M. Muhibullah, "A non-isolated bidirectional high gain integrated multiport converter for grid tied solar PV fed telecom load," *IET Power Electron.*, vol. 16, no. 5, pp. 828–842, Apr. 2023, doi: 10.1049/pel2.12426.
[29] V. Sheeja and R. Kalpana, "Power flow management of a solar PV and battery powered telecom load with bidirectional grid power exchange," in *Proc. IEEE 4th Int. Conf. Comput., Power Commun. Technol. (GUCON)*, Sep. 2021, pp. 1–6.
[30] *IEEE Recommended Practice and Requirements for Harmonic Control in Electric Power Systems*, IEEE Standard 519, 2014.

V. SHEEJA received the B.Tech. degree in electrical and electronics engineering from the University of Calicut, Kerala, in 2000, and the M Tech. degree in energy studies from the Indian Institute of Technology Delhi, Delhi, India, in 2009. She is currently pursuing the Ph.D. degree with the National Institute of Technology, Karnataka, Surathkal, India. She is also an Assistant Professor with the Department of Electrical and Electronics Engineering, LBS College of Engineering, Kasaragod. Her research interests include solar PV integration to grid, wind energy conversion systems, and power quality.

R. KALPANA (Senior Member, IEEE) received the bachelor's degree in electrical and electronics engineering from Madras University, Chennai, India, in 1998, the master's degree in power systems form Anna University, Chennai, in 2000, and the Ph.D. degree in electrical engineering from the Indian Institute of Technology Delhi, New Delhi, India, in 2012. She is currently an Assistant Professor with the Department of Electrical and Electronics Engineering, National Institute of Technology Karnataka, Surathkal, Mangaluru, India. Her research interests include power quality studies, power electronics applications to power systems, renewable energy, and energy management studies.

UMASHANKAR SUBRAMANIAM (Senior Member, IEEE) was an Associate Professor with VIT Vellore, a Senior Research and Development Engineer, and a Senior Application Engineer in the field of power electronics, renewable energy, and electrical drives. He is currently with the Renewable Energy Laboratory, College of Engineering, Prince Sultan University, Saudi Arabia. He has more than 15 years of teaching, research, and industrial research and development experience. He has published more than 250 research articles in national and international journals and conferences. He has also authored/coauthored/contributed 12 books/chapters and 12 technical articles on power electronics applications in renewable energy and allied areas. He is a member of IACSIT, IDES, and ISTE. He was an Executive Member, from 2014 to 2016, and the Vice Chair of the IEEE MAS Young Professional, from 2017 to 2019, by the IEEE Madras Section. He received the Danfoss Innovator Award-Mentor, from 2014 to 2015 and from 2017 to 2018, and the Research Award from VIT University, from 2013 to 2018. He has taken charge as the Vice Chair the IEEE Madras Section and the Chair the IEEE Student Activities, from 2018 to 2019. He is an Editor of *Heliyon* (Elsevier) journal. He also received the INAE Summer Research Fellowship, in 2014. Under his guidance, 24 P.G. students and more than 25 U.G. students completed the senior design project work. Also, six Ph.D. scholars completed doctoral thesis as a Research Associate. He is also involved in collaborative research projects with various international and national level organizations and research institutions.

DHAFER J. ALMAKHLES (Senior Member, IEEE) received the B.E. degree in electrical engineering from the King Fahd University of Petroleum and Minerals (KFUPM), Dhahran, Saudi Arabia, in 2006, and the master's (Hons.) and Ph.D. degrees from The University of Auckland, New Zealand, in 2011 and 2016, respectively. Since 2016, he has been with Prince Sultan University (PSU), Saudi Arabia. He is currently an Assistant Professor with the Department of Communications and Networks Engineering. He is also the Director of the Science and Technology Unit and the Leader of the Renewable Energy Laboratory, PSU. He has authored many published articles in the area of control systems. His research interests include the hardware implementation of control theory, signal processing, networked control systems, nonlinear control design, unmanned aerial vehicle (UAV), and renewable energy. He has served as a Reviewer for many journals, including IEEE TRANSACTIONS ON FUZZY SYSTEMS, IEEE TRANSACTIONS ON CONTROL OF NETWORK SYSTEMS, IEEE TRANSACTIONS ON INDUSTRIAL ELECTRONICS, IEEE TRANSACTIONS ON CONTROL SYSTEMS TECHNOLOGY, IEEE CONTROL SYSTEMS LETTERS, and the *International Journal of Control*.